Stationary X-ray Tomography for Hemorrhagic Stroke Imaging - Sampling and Resolution Properties

A. Lopez-Montes[a*], T. McSkimming[a,b], W. Zbijewski[a], J. H. Siewerdsen[a],

C. Delnooz[b], A. Skeats[b], B. Gonzales[b], A. Sisniega[a*]

[a] Department of Biomedical Engineering, Johns Hopkins University, Baltimore, MD 21205
[b]Micro-X LLC, A14 6 MAB Eastern Promenade, Tonsley, Australia 5042

ABSTRACT

Hemorrhagic stroke accounts for up to 20% of all stroke cases, and requires a treatment pathway drastically different to ischemic stroke. Prompt triage is therefore crucial and often only attainable with neuroimaging for intracranial hemorrhage (ICH) evaluation, for which MDCT is the frontline modality. Availability of ICH dedicated imaging in the pre-hospital setting, with portable CT systems, would facilitate early ICH diagnosis. However, current CT or cone-beam CT (CBCT) approaches often use conventional x-ray sources mounted on a rotating gantry limiting their minimum weight and footprint. Recent advances on cold-cathode, compact x-ray sources, based on carbon nanotube (CNT) technology, enable the development of ultra-compact designs based on source-array arrangements on stationary configurations. However, such geometrical arrangements show limited angular sampling, and sparse, non-stationary, volume sampling.

In this work we present first investigation of geometric configuration and effects of 3D sampling pertinent to the task of ICH detection on an ultra-portable stationary CBCT for ICH imaging. The baseline configuration included 31 CNT sources on a curved array illuminating a curved panel detector (871 mm length), on a compact geometrical configuration (SDD = 690 mm). Metrics of sampling completeness, sampling density, and MTF shape and band-width integral were explored for configurations varying in source angular span (30°-170°), source array and detector curvature radius (250 mm to flat), use of 2D matrix source arrangements, and multi-acquisition protocols. The results show that sufficient sampling and resolution can be achieved with a combination of moderate curvature (~450 mm radius) of the source array and detectors, with better sampling properties for approximately matched curvature radii (up to 30% BWI improvement). Improved image quality was demonstrated with configurations featuring matrix source arrangements in combination with multi-acquisition protocols (around a 6% of improvement in sampling completeness).

Keywords: Brain imaging, CBCT, Tomosynthesis.

1. INTRODUCTION

Intracranial hemorrhage (ICH) presents a medical emergency often caused by head trauma or hemorrhagic stroke [1]. ICH accounts for up to 20% of all strokes [2], affecting 2 million people/year [3]. Promising therapeutic options have opened for treatment of acute ICH, involving aggressive supportive care and reversal of coagulopathy [4], with greater benefit for immediate treatment start, following the concept of "time is brain" [4]. Effective triage between hemorrhagic and ischemic stroke, based on neuroimaging, should be done as early as possible, preferably in the ambulatory or emergent, pre-hospital setup. To meet this need for pre-hospital imaging, several approaches to portable systems have been proposed in previous work, often based on cone beam CT (CBCT) designs some suitable to installation on mobile units [5], or the emergency room [6]. Such designs were often based on conventional CT or CBCT designs with enhanced portability, but required a rotating gantry system and used conventional x-ray sources that limited their portability and footprint. Recent advances in cold-cathode x-ray sources, such as those based on carbon-nanotube technologies (CNT), yielded improved stability and durability, and allowed the design of compact, light-weight sources that can be combined into linear or matrix arrangements [7]. Such arrangements can be integrated into stationary systems with extremely compact acquisition geometry and simple mechanical design, with recent examples in baggage inspection [7] and dental imaging [8]. Further reduction in system

* asisniega@jhu.edu; alopezm2@jhmi.edu

7th International Conference on Image Formation in X-Ray Computed Tomography,
edited by Joseph Webster Stayman, Proc. of SPIE Vol. 12304, 123040P
 · 0277-786X · doi: 10.1117/12.2646858

footprint could be attained in combination with novel curved detector designs. However, the capability of such systems to provide sufficient image quality for ICH visualization remains an open question, largely attributable to limited angular sampling; sparse, non-stationary, volume sampling; and effects of scatter in such compact configurations.

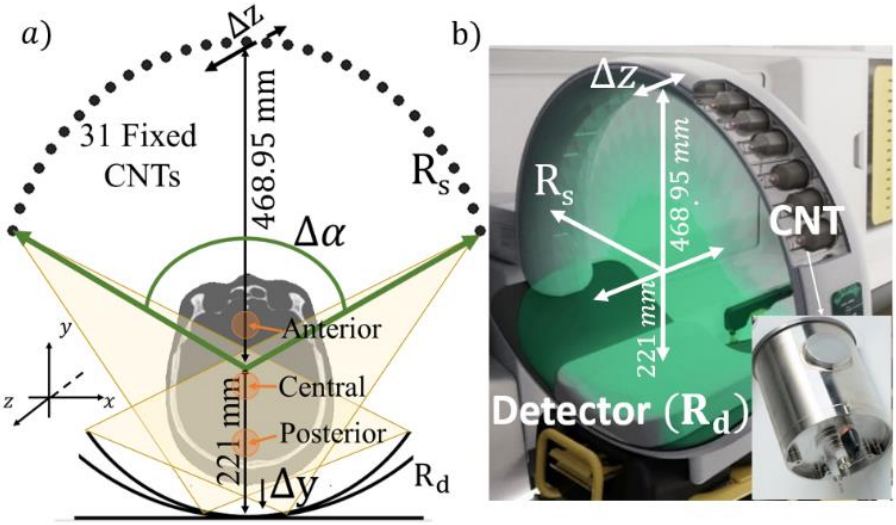

Fig. 1. a) Schematic representation of the stationary scanner configuration, featuring a curved 1D array (with extension to 2D matrix configurations) of CNT sources placed in opposition to a static flat-panel detector with variable curvature. The scanner configuration was optimized as a function of the variable parameters listed in the schematics ($\Delta\alpha$, RD, Rs, Δz, Δy). b) Artistic depiction of an example configuration of the stationary head scanner, featured as installed on an ambulance or mobile stroke unit. The CNT sources (see detail) are arranged in a curved array opposed to a curved flat-panel detector, following the general configuration in a).

In this work we present first investigation of geometric configuration and effects of 3D sampling pertinent to the task of ICH detection on an ultra-portable stationary CBCT for ICH imaging, designed for installation in mobile setups (Fig. 1B). Sampling, artifacts, and spatially-varying, directional, image resolution were characterized for a range of system configurations. Alternative linear and matrix source arrays and multi-exposure acquisition protocols were evaluated in simulation studies.
egin the Introduction two lines below the Keywords. The manuscript should not have headers, footers, or page numbers. It should be in a one-column format. References are often noted in the text[1] and cited at the end of the paper.

2. METHODS

2.1 Simulation setup for system optimization.

The configuration of the stationary head CBCT is illustrated in Fig.1A. The design included 31 CNT x-ray sources arranged along a curved array, at equiangular increments. The source arrangement was placed in direct opposition to a curved flat-panel detector of 837 mm size in the lateral direction (x) and 421 mm in the superior-inferior (SI) direction (z), with 1395 x 702 pixels (0.6 mm x 0.6 mm pixel size). The center of the world coordinate system was placed at the center of the patient head. To allow sufficient space for positioning of the head on a head rest, the center was placed 221 mm away from the detector surface (analogous to the axis-to-detector distance – ADD – often invoked in conventional CBCT). The distance between the center of the coordinate system and the source array (viz., source-to-axis distance – SAD – in CBCT) was set to 469 mm, yielding a source-to-detector distance (SDD) of 690 mm, compatible with the stringent footprint requirements for on-board systems on mobile medical units.

Variable parameters in the optimization studies included: i) the curvature of the source array, denoted Rs, defined as the radius of the circumference arc followed by the array (Fig. 1A), and ranging from a linear array with Rs = ∞ to a compact curved array with Rs = 250 mm; ii) the detector curvature, denoted Rd (Fig. 1A), defined in an analogously to Rs, and ranging from a conventional flat-detector configuration (Rd = ∞) to a curved detector with Rd = 250 mm, while maintaining a constant length of 837 mm for the curved segment; and, iii) the angular span of the source array (Δα, see Fig. 1A) varied between 30° and 165° for a nominal source curvature of Rs = 469 mm (resulting in an arrangement centered at the origin of coordinates).

Configurations featuring matrix source arrangements in the form of two parallel curved arrays were simulated by translating each source in consecutive pairs in opposite directions along the SI axis (z) by a distance Δz ranging from 0 mm to 40 mm. Even (odd) sources were shifted towards positive (negative) z values.

Final configurations studied potential improvement from multi-acquisition protocols in which two datasets were obtained with a linear translation of the patient head in the antero-posterior (AP) direction (y) between 0 mm and Δy = 20 mm.

Optimization studies used a realistic simulator for primary signal [9], including polychromatic source spectra and energy-dependent material properties and detector response. Current studies were focused on pure sampling effects and did not include effects of x-ray scatter and system noise. The simulations used a head phantom imaged with high-resolution MDCT and featuring natural bone skull and sinuses structure and a homogeneous brain parenchyma with 0 HU attenuation. ICH was simulated with synthetic spherical bleed inserts with 60 HU contrast and 8 mm diameter, placed on a regular grid lattice with 16 mm spacing. The head was positioned with a 45° tilt along the z axis, aligning the central scan plane with a plane joining the posterior skull base with a frontal brain region. The x-ray source spectrum was simulated with the Spektr [10] TASMICS model for 100 kV (+2 mm Al, + 0.2 mm Cu added filtration). The detector model featured a flat-panel detector with a 250 mg/cm2 CsI:Tl scintillator.

2.2 Model Based Iterative Reconstruction.

Image reconstruction used a Penalized Weight Least Squares (PWLS) algorithm that can accommodate non-conventional sampling patterns [11], such as those arising in the proposed stationary configurations. Reconstructions were obtained minimizing the following PWLS cost-function. [12]

$$\mu = \arg_{\mu \geq 0} \min \left|\left|\mathbf{A}\mu - l\right|\right|_w^2 + \beta R(\mu) \quad (1)$$

where **A** denotes the projection operator, l are the raw line integrals, and w are stochastic weighting terms that minimize the contribution of noisy measurements. In this work we model w with the raw measurements, commonly used as a surrogate of measurement variance. To avoid sharp transitions in presence of truncation, w values adjacent to the detector lateral edge were tapered following a ERF function with σ = 2 mm[13]. $R(\mu)$ is an image roughness quadratic regularization term weighted by the scalar β, set to a nominal value of $\beta = 10^{-3}$. To induce consistent regularization across configurations, the value of σ was scaled by a factor of 2 for multi-acquisition protocols to compensate for the double number of views included in such protocols. Reconstructions were obtained on a 390 x 696 x 696 voxels grid (0.5 mm isotropic size) for 1000 iterations.

2.3 Metrics of sampling completeness and image quality.

Imaging performance was assessed in terms of voxel sampling density, sampling completeness, and local spatial resolution properties. Local sampling density was estimated as the number of rays (i.e. source views) contributing to an individual voxel j, normalized by a nominal value of 360 for a full conventional CBCT scan, yielding $\rho_{samp}(j) = N_{view}(j)/360$.

Effects of limited angular sampling were evaluated by the local sampling completeness (ΔA), estimated as the angular span covered by the rays contributing to a voxel, normalized by the 180° span required for artifact-free tomographic reconstruction. Defining θ_0 and θ_f as the angle between the x axis and the first and last views contributing to voxel j, completeness was computed as $\Delta A(j) = |\theta_0(j) - \theta_f(j)|/180$.

While spatial resolution properties of the volume obtained with model-based iterative reconstruction methods are non-stationary and generally difficult to predict, approximations invoking local stationarity have been shown to provide accurate estimations of the local MTF in PWLS with locally smooth (quadratic) penalty designs. Local MTF was estimated using the model in [14], which for a voxel j inside a homogeneous region is given by:

$$MTF_j = \frac{\mathcal{F}\{ROI_j\{\mathbf{A^T B W A} e_j\}\}}{\mathcal{F}\{ROI_j\{\mathbf{A^T W A} e_j + \mathbf{R} e_j\}\}} \quad (2)$$

where $\mathbf{A^T}$ is the backward projection operator, **W** is the diagonal matrix containing the PWLS weighs, and **R** is the Hessian of the PWLS quadratic penalty. **B** is a system blurring factor, obtained as in [14], and e_j represents a Kronecker delta at voxel j. To evaluate the resolution properties across configurations we qualitatively assessed the shape of the resulting

MTF, while quantitative assessment was obtained with a version of a modified version of the Band Width Integral (BWI) in [15]:

$$\mathrm{BWI} = 100 \times \frac{\int_{\omega_0}^{\omega_f} MTF^2 d\omega}{\int_{\omega_0}^{\omega_f} d\omega^2} \tag{3}$$

The integration limits were set to ω_0 = 0.2 mm^{-1} and ω_f = 0.6 mm^{-1} pertinent to visualization of mid-size hemorrhage modelled with Gaussian kernel with σ = 4 mm. Sampling and resolution metrics, were evaluated for three regions of interest (ROIs), at the anterior, central, and posterior regions of the brain (see Fig. 1A).

3. RESULTS

3.1 Stationary Tomography Geometrical Configuration.

Fig. 2A illustrates voxel sampling completeness (ΔA) for the three ROIs as a function of the angular span ($\Delta\alpha$) of the source array, for a fixed R_s = 469, and three detector curvatures: i) a flat-panel configuration ($R_d = \infty$); ii) a moderate curvature (R_d = 650 mm); and iii) a curved, compact, detector (R_d = 450 mm).

Large values of $\Delta\alpha$ resulted in significant the truncation of the anterior regions of the head for certain views, evidenced as a reduction of ΔA for $\Delta\alpha > 80°$ and $\Delta\alpha > 100°$ for $R_d = \infty$ in the anterior and central ROIs, respectively. Curved detectors offered improved sampling completeness for those regions, showing a plateau at $\Delta A \cong 0.7$ for $\Delta\alpha > 120°$, for the anterior ROI, compared to $\Delta A \cong 0.6$ with $R_d = \infty$, with slight better performance for R_d = 450 mm. A similar trend was observed for the central and posterior ROIs.

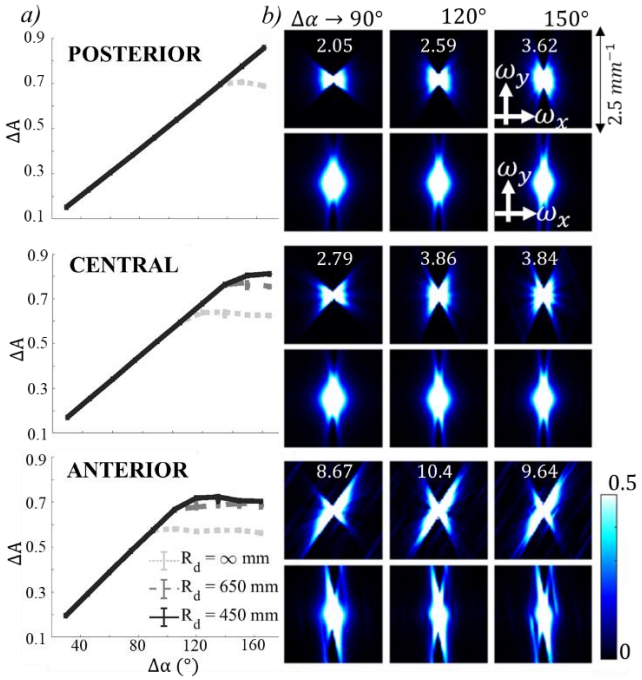

Fig. 2. ***a)*** Voxel sampling completeness as a function of sources angular span, for three detector curvatures, $R_d = \infty$, R_d = 450 mm, and R_d = 650 mm. Curves represent the mean value while error bars mark the 80% confidence interval within the ROI. ***b)*** Axial and coronal MTF for varying source angular span at a fixed detector curvature of R_d = 450 mm. Numerical values in the MTFs show the mid-band BWI.

MTF distributions in the axial and coronal planes are shown in Fig. 2B, for R_d = 450 mm, for the three ROIs, and for angular spans around the region where sampling completeness becomes flat in Fig. 2A: $\Delta\alpha$ of 90°, 120°, and 150°. As hinted by trends in ΔA, we observe a reduction of the MTF shade region between $\Delta\alpha$ = 90° and $\Delta\alpha$ = 120°, yielding an increase of 10%, 30%, and 25% in mid-band integrated MTF for the anterior, central, and posterior ROIs, respectively.

The gains in directional resolution are less apparent for angular span $\Delta\alpha > 120°$, except for the posterior region, that sees increased completeness and a reduction of the MTF shade region. However, such gains come accompanied by the appearance of high-frequency structures in the frontal region, associated to streak artifacts from increased truncation of intricate frontal maxillofacial bone anatomy.

Fig. 3 illustrates the impact of varying the curvature of the detector and arc of sources for a configuration with an arc length of the compromise setup with $\Delta\alpha = 120°$ arising from results in Fig. 2. The range of curvature explored ranged for very compact arrangements ($R_s = R_d = 250$ mm), to extended arrangements pertinent to linear tomosynthesis ($R_s = R_d = \infty$) The results in Fig. 3A suggest increased sampling density and completeness for very compact configurations, increased truncation of anterior bone regions result in high frequency streak patterns in the MTF that can be observed as increased high frequency artifacts and non-uniformity in Fig. 3C (top row). Consistent with monotonic reduction of sampling completeness (Fig 3A) with increased R_s and R_d, Fig. 3B show a similar loss of frequency information for such combinations of large R_s and R_d. For example, using a linear tomosynthesis configuration leads to a reduction of ~10% mid-band MTF compared to a moderate configuration with $R_s = R_d = 450$ mm. This loss of information for very large radii resulted in limited angle artifacts usually observed in tomosynthesis imaging (see Fig. 3C). The results in Fig. 3 suggest that approximate match of the detector and source curvature is associated to better sampling properties, with mid-band MTF increases up to 25%, compared to configurations with large mismatch between detector and source curvatures.

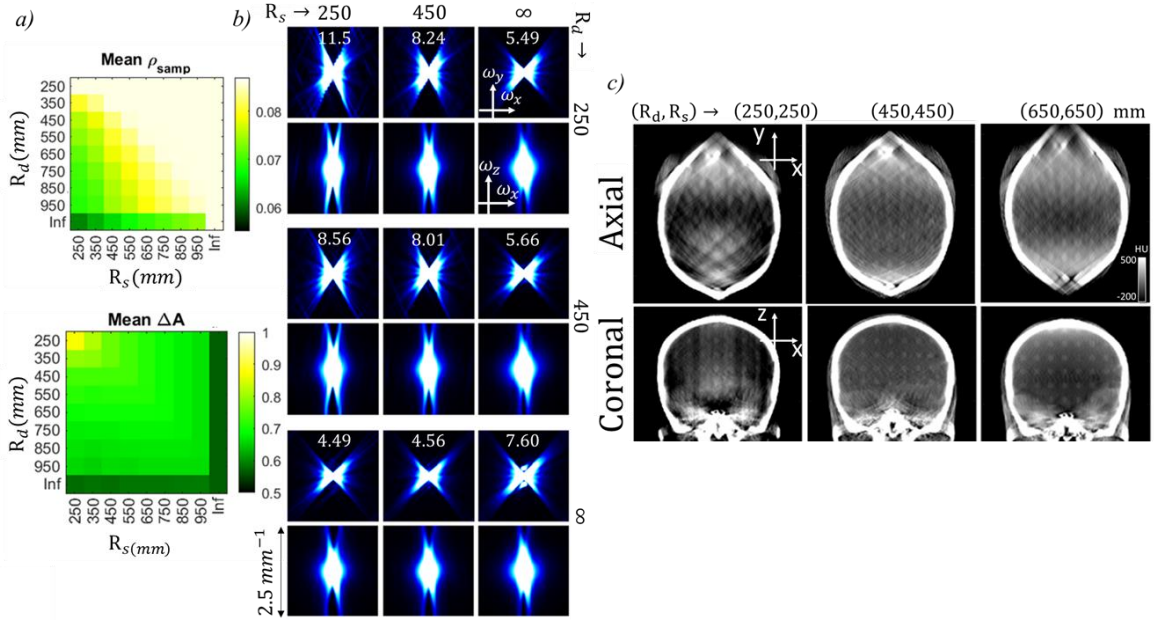

Fig. 3. *a)* Mean sampling density and angular span for the anterior ROI b) MTF as a function of sources and detector curvature for the anterior ROI. Numerical values in the MTFs correspond to the BWI along a mid-frequency band (0.2 mm^{-1} - 0.6 mm^{-1}). c) Reconstructed images for different combinations of sources and detector curvatures, for a very compact, curved geometry (left), a moderately curved geometry (middle), and a configuration with a linear array of sources and a flat-detector yielding a linear tomosynthesis configuration.

3.2 Array vs matrix source configurations.

Figure 4 compares MTF and image results for 1-dimensional array and matrix configurations of the source arrangement. Matrix arrangements with an interleaved distribution of sources resulted in increased resolution in the SI direction, as evidenced by the reduction of the shade region in the coronal MTF and reduction of cone-beam artifacts above and around the orbital structures at the anterior region of the brain. However, such improvements were accompanied by a reduction in the overall contrast of the blood inserts, attributable to a reduction of local sampling density across the brain region.

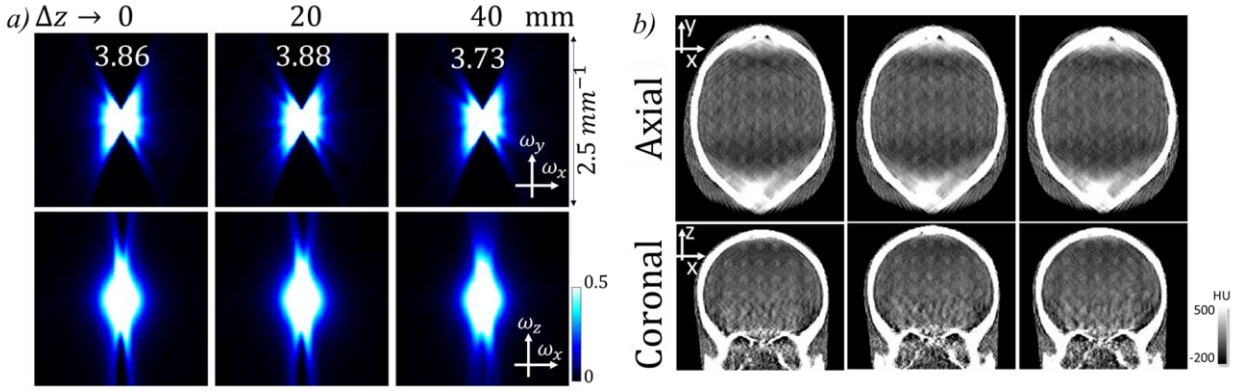

Fig. 4. Results of array (Δz = 0 mm) vs matrix source configurations with Δz = 20 mm and Δz = 40 mm. ***a)*** MTF for the central region of the brain. Numerical values in the MTFs correspond to the BWI along a band pass filter between 0.2 mm^{-1} and 0.6 mm^{-1}. ***b)*** Reconstructed images for different distance between parallel arcs. Slight improvement in shading artifacts attributable to cone beam effects can be observed at frontal regions close and above the orbital bone for matrix arrangements and large separation. However, reduced shading was associated to reduced contrast for bleed inserts at central regions of the brain.

3.3 Multi-acquisition protocol.

As illustrated in previous results, one limiting factor for image quality is the increased truncation of bone anatomy and reduced sampling density at anterior regions of the head for compact configurations, causing high-frequency streak-like artifacts in the reconstructed images. As shown in Fig. 5, the sampling completeness is increased by ~6% for the multi-acquisition protocol with Δy > 12 mm. This improvement leads to better visualization of blood inserts, particularly in the anterior region of the brain, as seen in Fig. 5B.

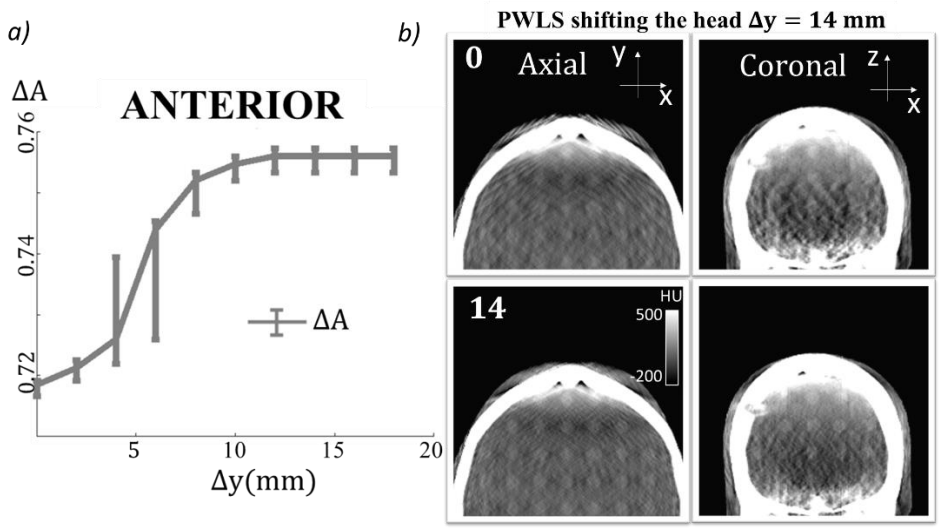

Fig. 5. Performance of the multi-acquisition protocol as a function of the head shift distance. ***a)*** Sampling completeness as a function of head translation. ***b)*** Anterior region of the reconstructed images for the single acquisition protocol (top) and for a multi-acquisition protocol with $\Delta y = 14\ mm$.

4. DISCUSSION AND CONCLUSION

This work studied the tradeoffs in sampling and resolution for a comprehensive range of geometrical configurations in stationary tomographic systems for imaging of hemorrhagic stroke. The results show that sampling and resolution sufficient for the task of ICH detection can be achieved with a combination of curved array sources arrangements and curved panel detectors. Better sampling properties was observed for approximately matched curvature radii, as evidenced by increase in sampling completeness and density aggregated metrics as well as increases in radial homogeneity of the MTF distributions. Improved image quality can be achieved by combination of matrix source configurations and multi-

acquisition protocols. The studies presented in this work did not consider the effects of x-ray scatter and quantum and instrumentation noise on image quality and focused solely on effects of sampling and frequency response. Scatter and noise are expected to pose a complex multi-variate scenario, in combination with sampling considerations, and are the subject of ongoing work.

5. ACKNOWLEDGEMENTS

This work was supported by academic-industry partnership between the Australian Stroke Alliance, Micro-X Ltd., and Johns Hopkins University.

REFERENCES

[1] Ghajar, J. Traumatic brain injury. The Lancet, 356(9233), 923-929. (2000).
[2] Feigin, V. L., Lawes, C. M., Bennett, D. A., Barker-Collo, S. L., and Parag, V. (2009). Worldwide stroke incidence and early case fatality reported in 56 population-based studies: a systematic review. The Lancet Neurology, 8(4), 355-369.Krishnamurthi, et al. Lancet Glob. Heal. 1(5), e259–e281 (2013).
[3] Cordonnier, C., Demchuk, A., Ziai, W., and Anderson, C. S. (2018). Intracerebral haemorrhage: current approaches to acute management. The Lancet, 392(10154), 1257-1268.Ebinger, M. et al., JAMA311(16), 1622–1631 (2014).
[4] Wu, P., Sisniega, A., Stayman, J. W., Zbijewski, W., Foos, D., Wang, X., Khanna, N., Aygun, N., Stevens, R. D., and Siewerdsen, J. H. (2020). Cone-beam CT for imaging of the head/brain: Development and assessment of scanner prototype and reconstruction algorithms. Medical Physics, 47(6), 2392–2407. https://doi.org/10.1002/mp.14124
[5] Gonzales, B., Spronk, D., Cheng, Y., Tucker, A. W., Beckman, M., Zhou, O., and Lu, J. (2014). Rectangular fixed-gantry CT prototype: combining CNT X-ray sources and accelerated compressed sensing-based reconstruction. IEEE Access, 2, 971-981.
[6] Spronk, D., Luo, Y., Inscoe, C., Billingsley, A., Lee, Y. Z., Lu, J., and Zhou, O. (2020, March). Feasibility of a stationary head CT scanner using a CNT x-ray source array. In Medical Imaging 2020: Physics of Medical Imaging (Vol. 11312, pp. 773-780). SPIE.
[7] Wu, P., Sisniega, A., Uneri, A., Han, R., Jones, C., Vagdargi, P., ... and Siewerdsen, J. (2021). Using uncertainty in deep learning reconstruction for cone-beam CT of the brain. arXiv preprint arXiv:2108.09229.
[8] Punnoose, J., Xu, J., Sisniega, A., Zbijewski, W., & Siewerdsen, J. H. (2016). spektr 3.0—A computational tool for x-ray spectrum modeling and analysis. Medical physics, 43(8Part1), 4711-4717.
[9] Stayman, J. W., Capostagno, S., Gang, G. J., and Siewerdsen, J. H. (2019). Task-driven source–detector trajectories in cone-beam computed tomography: I. Theory and methods. Journal of Medical Imaging, 6(2), 025002.
[10] Sisniega, A., Stayman, J. W., Capostagno, S., Weiss, C. R., Ehtiati, T., and Siewerdsen, J. H. (2021). Accelerated 3D image reconstruction with a morphological pyramid and noise-power convergence criterion. Physics in Medicine & Biology, 66(5), 055012.
[11] Zhang, Y., Chan, H. P., Sahiner, B., Wei, J., Ge, J., Zhou, C., and Hadjiiski, L. M. (2009). Artifact reduction methods for truncated projections in iterative breast tomosynthesis reconstruction. Journal of computer assisted tomography, 33(3), 426.
[12] Wang, W., Gang, G. J., Siewerdsen, J. H., and Stayman, J. W. (2019). Predicting image properties in penalized-likelihood reconstructions of flat-panel CBCT. Medical Physics, 46(1), 65–80. https://doi.org/10.1002/mp.13249.
[13] Wagner, R. F., Brown, D. G., and Pastel, M. S. (1979). Application of information theory to the assessment of computed tomography. Medical physics, 6(2), 83-94.